Research Square

Preprints are preliminary reports that have not undergone peer review.
They should not be considered conclusive, used to inform clinical practice,
or referenced by the media as validated information.

Discovery and Exploration of Mechanistically Distinct FtsZ Compounds Inhibiting Mycobacterial Cell Division

Shawn Chen

shuo.chen@ghddi.org

Global Health Drug Discovery Institute

Jinglan Wang

Qiping Hu

Global Health Drug Discovery Institute

Heng Wang

Global Health Drug Discovery Institute

Genhui Xiao

Global Health Drug Discovery Institute

Heli Jiang

Global Health Drug Discovery Institute

Yueyang Xu

Global Health Drug Discovery Institute

Yu Chang

Global Health Drug Discovery Institute

Miaomiao Pan

Global Health Drug Discovery Institute

Mengyun Zhang

Global Health Drug Discovery Institute

Liangliang Zhou

Global Health Drug Discovery Institute

E Liang

Global Health Drug Discovery Institute

Yuan Zhang

Global Health Drug Discovery Institute

Ruiyuan Liu

Institute of Microbiology, Chinese Academy of Sciences

Jinzhi Wu

Global Health Drug Discovery Institute

Chi-Kin Chan
Global Health Drug Discovery Institute
Jinjiang Guo
Global Health Drug Discovery Institute https://orcid.org/0000-0002-9157-2199
Renhe Liu
Global Health Drug Discovery Institute
Lan Xu
Global Health Drug Discovery Institute
Zhiyang Zou
Global Health Drug Discovery Institute
Rumin Zhang
Yu Lu
Beijing Chest Hospital
Tanya Parish
Department of Tropical Disease Biology, Liverpool School of Tropical Medicine
Junhao Zhu
Institute of Microbiology, Chinese Academy of Sciences

Article

Keywords: FtsZ, Mycobacterial cell division, high-throughput screening, inhibition mechanism, bacterial cytological profiling

Posted Date: November 6th, 2026

DOI: https://doi.org/10.21203/rs.3.rs-11584760/v1

License: This work is licensed under a Creative Commons Attribution 4.0 International License.
Read Full License

Additional Declarations: There is **NO** Competing Interest.

Abstract

The *Mycobacterium tuberculosis* (Mtb) complex causes disease in humans and animals, underscoring the need for antitubercular agents with novel mechanisms. We investigated FtsZ, a conserved essential component of the mycobacterial divisome, by screening anti-TB compounds for FtsZ binding, GTPase inhibition, and impact on cell morphology. Hits were triaged as thermal stabilizers or destabilizers of MtbFtsZ based on thermal-shift profiles and validated using CRISPRi *ftsZ* knockdown in *Mycobacterium bovis* BCG. Bacterial cytological profiling and orthogonal biochemical and cell-based assays, including hydrogen-deuterium exchange mass spectrometry, dynamic light scattering, and Z-ring imaging, supported that the compounds had distinct effects on FtsZ and the divisome. We explored several chemotypes through analog synthesis and used the GAC15 series to investigate cellular mechanisms. Amide hydrolysis and nitro-group reduction were implicated in loss of GAC15 activity in BCG. These compounds provide tools for dissecting FtsZ dynamics and divisome function and a framework for discovering novel anti-TB agents.

Introduction

The bacterial divisome is a multi-protein apparatus that orchestrates cytokinesis. In model organisms such as *Escherichia coli* and *Bacillus subtills*, more than 30 proteins are reported to directly participate in the cytokinetic process.[1−4] Among these, FtsZ, a distant bacterial homolog of the eukaryotic cytoskeletal protein tubulin, is the centerpiece.[5−7] Divisome assembly begins with FtsZ polymerization to form a ring-like structure (Z-ring) at the midcell, marking the future division site. The Z-ring subsequently serves as a scaffold for recruiting additional divisome components, tethering the core machinery to the cytoplasmic membrane. Treadmilling of FtsZ filaments, with growth at one end and contraction at the other, then drives septal cell wall synthesis at the division plane,[8,9] ultimately mediating cell constriction. The strong dynamics of FtsZ and divisome protein interactions regulate bacterial cell division.

FtsZ is conserved across nearly all bacteria and shares functional homology with eukaryotic tubulin, most notably at the nucleotide-binding site. However, the two proteins diverge substantially at the sequence level and in the polymer form.[10,11] FtsZ polymerization is governed by GTP; GTP-loaded monomers assemble into single-stranded polymers (protofilaments), and GTP hydrolysis powers filament treadmilling. Crystal structures of FtsZ homodimer and the cryo-EM structure of polymeric protofilaments have revealed a conserved, modular architecture and the conformational changes underlying Z-ring assembly and disassembly.[12−14] An FtsZ monomer folds into an N-terminal core domain (NTD) and a C-terminal core domain (CTD) connected by a short interdomain linker; the H7 helix of the NTD and the T7 loop of the CTD project toward the subunit interface. The composite GTPase active site forms at the interface between adjacent monomers, where the T7 loop of one subunit engages the GTP-binding pocket in the NTD of its neighbor. Hydrolysis of GTP to GDP within this composite pocket promotes FtsZ depolymerization, switching the protein structure from open to closed conformation. Beyond the CTD lies the C-terminal tail region (CTT), which consists of a disordered C-

terminal linker (CTL) followed by a short C-terminal conserved (CTC) peptide and a variable C-terminal extension. The CTC peptide adopts a structured conformation to bind membrane-anchoring proteins, thereby recruiting the Z-ring to the cytoplasmic membrane,[15,16] whereas the CTL acts as a flexible tether that modulates lateral interactions between FtsZ protofilaments and regulates polymer stability.[17–19] Collectively, these structural features enable the cooperative assembly, membrane tethering, and dynamic turnover of the Z-ring.

Because the divisome is essential, unique to bacteria, and not targeted by commercial antibiotics, in contrast to human tubulin targeted by many anticancer drugs, FtsZ and the other essential division proteins represent a promising yet largely underexploited avenue in the antimicrobial field. However, FtsZ-directed drug discovery has been hindered by two persistent challenges. First, many reported inhibitors were identified via phenotypic screening and therefore lack rigorous mechanism-of-action (MoA) validation, leaving their on-target engagement uncertain.[11,20–23] Second, this major cytoskeletal protein is perceived as less selective than other bacterial targets. Previously published FtsZ hits screened from synthetic libraries have a narrow therapeutic window, with only a few exceptions—notably the benzamide derivative PC190723,[24] whose optimized prodrug TXA709 has progressed into clinical trials to evaluate safety and efficacy against methicillin-resistant *Staphylococcus aureus*.[25]

Targeting the mycobacterial divisome offers a strategic advantage in drug discovery. *Mycobacterium tuberculosis* (Mtb)—the causative agent of tuberculosis—remains a critical public health threat globally. Mtb and related members of the complex—including the zoonotic pathogen *M. bovis* and its vaccine derivative *M. bovis* BCG—assemble a divisome that differs from that of conventional bacterial model organisms.[26,27] These architectural distinctions create opportunities for selective inhibitors that disrupt mycobacterial division while sparing the host microbiome. Moreover, the escalating burden of multidrug-resistant and extensively drug-resistant tuberculosis underscores the urgent need for chemotherapeutics with a novel MoA.

Antimycobacterial discovery targeting FtsZ began with the sequencing of the Mtb genome and the determination of FtsZ protein structures.[12] Although incremental progress has been made over years,[28–34] many reported compounds have not been fully validated,[35] partially due to the technical demands of mycobacteriology and the unique biology of the mycobacterial divisome. In this work, we have addressed these gaps by integrating CRISPRi-based target validation, orthogonal biophysical and biochemical assays, and bacterial cytological profiling (BCP). Using *M. bovis* BCG as a surrogate model, we identified structurally diverse compounds that engage the MtbFtsZ through distinct mechanisms—thermal destabilization, thermal stabilization, and potential disruption of divisome protein interactions—and demonstrated their on-target antimycobacterial activity, thereby exploring two FtsZ compound series. Our findings establish a framework for discovery of FtsZ-targeting compounds and provide new chemical tools for interrogating FtsZ in mycobacteria.

Results

Target validation and assay development

FtsZ is a housekeeping protein, and its amino acid sequence is identical or > 99% conserved across slowly growing mycobacterial species (SGM) (Supplementary Fig. 1; Supplementary Table 1). To assess the genetic vulnerability of FtsZ in *M. bovis* BCG Pasteur 1173P2 and to establish a cell-based validation system, we applied a CRISPR interference (CRISPRi) technology previously developed for mycobacteria.[36] We generated an anhydrotetracycline (ATc)-inducible *ftsZ* transcriptional knockdown strain, GH161, and queried its growth, post-knockdown viability, *ftsZ* mRNA and protein levels, and cell length with varied knockdown strengths (ATc concentrations) and durations (Fig. 1; Supplementary Fig. 2). At the cellular level, GH161 exhibited ATc-dependent growth inhibition (Fig. 1a, b) and cell elongation (Fig. 1c, d). Prolonged transcriptional knockdown induced by 100 ng/mL ATc reduced cell viability as measured by colony-forming units (CFU) (Fig. 1b). At the molecular level, upon 3 ng/mL ATc induction, *ftsZ* mRNA and FtsZ protein declined in a dose-dependent manner, though with markedly different kinetics: mRNA dropped by > 80% within 2 days, whereas protein remained at ~ 90% of baseline (Supplementary Fig. 2b, c). Further increasing ATc to 10 ng/mL reduced FtsZ protein to approximately two-thirds of baseline (~ 30% decrease). Notably, even at sub-inhibitory ATc concentrations (< 4 ng/mL), when the effects on growth and FtsZ protein level were minimal, cell length increased substantially relative to the uninduced control (Fig. 1c, d). These results establish two critical benchmarks for our FtsZ-directed screening strategy: first, that FtsZ is a vulnerable target in BCG, and second, that cell elongation is a sensitive phenotypic readout of reduced FtsZ function that precedes growth inhibition or loss of viability caused by FtsZ depletion.

Guided by these observations, we leveraged inducible CRISPRi-mediated *ftsZ* suppression (termed *ftsZ*-KD hereafter) in GH161 to evaluate the cellular on-target activity of FtsZ-directed compounds, a strategy proposed to study chemical-genetic interactions in *Mycobacterium*.[37] Like the determination of the minimum inhibitory concentration (MIC, typically for 90% growth inhibition) of a test compound, an MIC50-shift assay estimates a compound's target engagement under induced versus uninduced *ftsZ*-KD conditions by comparing the concentrations required to produce 50% growth inhibition. We noticed that at least four antimycobacterial antibiotics with known MoAs: isoniazid, moxifloxacin, D-cycloserine, and capreomycin produced no or non-significant MIC50-shift when *ftsZ*-KD was induced in GH161 (Supplementary Fig. 2d). Next, we tested several reported mycobacterial whole-cell active FtsZ inhibitors (Supplementary Fig. 3), including SB-RA-2001 and SRI-3072 (MMV1633967). SB-RA-2001 is a noncytotoxic taxane,[30,38] a complex natural product derivative that binds to tubulin in an open pocket overlapping with bacterial FtsZs. A recent structural study uncovered ligand recognition at this pocket,[14] suggesting SB-RA-2001 might engage FtsZ in the cells. The MIC50-shift assay indicated that *ftsZ*-KD sensitizes GH161 to SB-RA-2001 in a dose dependent manner and that sub-inhibitory ATc concentration (2 ng/mL) lowered the SB-RA-2001's MIC50 more than half (3.6 to 1.2 μM, Fig. 1e). SRI-3072 was originally identified as a potent anti-TB compound with sub-micromolar whole-cell activity and was reported to inhibit MtbFtsZ polymerization and GTPase activity in vitro at concentrations > 40 μM,[28] which was also confirmed by our assays described below. However, the cell-based assay indicated that

while SRI-3072 was active against BCG, it might not exclusively inhibit FtsZ function, as the MIC50 shifted less than 2-fold in the induced GH161 (Fig. 1f). Both SB-RA-2001 and SRI-3072 visibly elongated the BCG cells (Fig. 1g), with the former being more statistically significant (n = ~ 100, 1.8 µm increase).

To directly screen for FtsZ inhibitors, we purified MtbFtsZ protein (Supplementary Fig. 4) and developed two orthogonal biochemical assays: a GTPase inhibition assay that measures MtbFtsZ-dependent GTP hydrolysis, and a thermal unfolding assay (Thermal Shift Assay, TSA) that detects ligand-induced changes in MtbFtsZ protein stability.[39–41] The TSA was implemented as a dye-based differential scanning fluorimetry assay in a 384-well PCR plate format, making it accessible, low-cost, and suitable for high-throughput screening (HTS). As shown in Fig. 1H, a GTP hydrolysis assay demonstrated that SRI-3072 inhibited MtbFtsZ's GTPase activity with an IC_{50} of 68 µM. Corroborating this in the TSA experiment, SRI-3072 interacts with MtbFtsZ as a destabilizer, decreasing the melting temperature (T_m) by 3.9°C at 100 µM (Fig. 1i). By contrast, the nonhydrolyzable substrate analog GTPγS increased the T_m of MtbFtsZ, consistent with thermal stabilization upon binding (Supplementary Fig. 4c). We interpret negative and positive changes in melting temperature (ΔT_m) as distinct ligand-dependent responses of MtbFtsZ, both of which would have functional consequences. We did not obtain a valid biochemical readout for SB-RA-2001 because it was poorly soluble in biological assay buffers (Supplementary Fig. 5).

In addition, we also tested and explored a recently reported MtbFtsZ inhibitor series, sulindac sulfide (SS) and its derivatives,[32] including reported compound 18 (named SS-18 herein) which inhibits MtbFtsZ polymerization and Mtb growth with IC_{50}s of ~ 40 µM and ~ 7.3 µM, respectively (Supplementary Fig. 4d, f). Like SRI-3072, SS-18 lowered the T_m of MtbFtsZ as measured by fluorometric TSA, indicating MtbFtsZ destabilization (Supplementary Fig. 4e). While all synthesized SS analogs induced noticeable negative ΔT_m in MtbFtsZ, they inhibited GTPase activity at high concentrations (IC_{50} ~58 µM to > 100 µM) and showed varying degrees of MIC50 shift with *ftsZ*-KD (Supplementary Fig. 4f, g). Nonetheless, subtle changes in the SS core afforded GDI-B029, which has reasonably good biochemical and cellular activities and appears on target in GH161. Collectively, these results attest that previously reported Mtb-active FtsZ compounds can be validated at the cellular level, supporting the utility of our system for hit triage and confirmation. Equally importantly, a range of MtbFtsZ-directed assays have enabled screening for novel mycobacterial cell divisome inhibitors.

Screening of whole-cell active collections for MtbFtsZ compounds

To establish a screening cascade for FtsZ-directed inhibitors in BCG and Mtb (Fig. 2a), we prioritized compound sets that were readily available, whole-cell active, and enriched for drug-like properties. We screened several proprietary anti-TB collections, including TB Alliance TBacs[42] (1,380 compounds), GlaxoSmithKline TB-actives[43] (2,111 compounds), the MMV Pandemic Response Box[44] (400 compounds), and an in-house GACtives set (~ 900 compounds), for a total of ~ 5,000 compounds. The libraries were screened using both TSA and GTPase inhibition assays. Primary hits were defined as

compounds that inhibited GTPase activity by ≥ 80% and/or produced an absolute thermal shift ($|\Delta T_m|$) > 1.5°C (Fig. 2b). As GTPase inhibition does not capture all possible modes of FtsZ modulation, and because a robust TSA response indicates direct ligand binding, compounds with significant thermal shifts (> 3°C) but weak or no GTPase inhibition were also advanced to secondary morphological screening. GH161 cells with very weak *ftsZ*-KD (ATc ~ 0.25 ng/mL) were treated with each hit at its MIC or, when MIC data were unavailable, at ~ 20 μM, and their cell lengths were measured by brightfield microscopy imaging and a bespoke imageJ macro script. Here, we adopted an empirical cutoff of a cell-length increment over 1 μm on compound treatment to prioritize hits for resupply. Figure 2c shows the repurchased or resynthesized compounds, and Table 1 and Supplementary Table 2 summarize the key assay data.

Among the confirmed hits, five compounds—TBC47a, GDI-8134, GDI-10399, TBC10, and MMV-1—showed negative ΔT_m values and were thus classified as thermal destabilizers, whereas five compounds—GDI-10455, GDI-10407, GDI-10458, GSK20a, and GAC15—showed positive ΔT_m values and were considered thermal stabilizers. Importantly, the destabilizers all inhibited MtbFtsZ GTPase activity after 16 h preincubation with purified protein, with IC_{50} values of ~ 40–60 μM in the assay containing 5 μM FtsZ. In contrast, the stabilizers showed more variable effects on GTPase activity. For example, GAC15, GSK20a, and related analogs increased the thermal stability of MtbFtsZ but did not significantly inhibit GTP hydrolysis (Fig. 2c; Table 1).

Confirmation and validation of MtbFtsZ screening hits

The resupplied compounds were subjected to orthogonal phenotypic and biochemical validations. Primary validation was with two methods: ≥2-fold MIC_{50} downshift upon mild *ftsZ*-KD (GH161 treated with 2 ng/mL ATc), and *in vitro* disruption of the dynamic FtsZ polymer assembly. The latter was measured by estimating the size distribution of MtbFtsZ polymers by dynamic light scattering (DLS) hydrodynamic radius (r_h) (Supplementary Fig. 6).[45,46] In a typical DLS reaction containing 4 μM MtbFtsZ protein and 60 μM GTP, MtbFtsZ completes a polymerization and depolymerization cycle in about 8 hours. Two tool compounds, SS-18 and GDI-B029, effectively delayed or inhibited FtsZ polymerization at 50 μM. The DLS assay is very sensitive to compound solubility; the effect of large or nonpolar FtsZ-hits cannot be accurately measured in this assay.

For an alternative or complementary assay to light scattering, we considered irregular Z-ring morphology a reliable cellular readout of FtsZ polymer disruption.[21] Because expression of MtbFtsZ in BCG from its native promoter was lethal in both our study and prior work,[47,48] we performed the Z-ring assay in an *M. smegmatis* strain expressing an MtbFtsZ-GFP fusion protein. In untreated cells, the Z-ring appeared normal, whereas most confirmed MtbFtsZ hits that were also active against *M. smegmatis* could cause abnormal Z-ring morphology (Fig. 2d). Both thermal stabilizers and destabilizers disrupt Z-ring formation or alter the localization of division proteins, supporting the conclusion that these hits screened with MtbFtsZ protein perturb FtsZ dynamics in cells.

We use TBC47a to illustrate the hit validation workflow (Fig. 2; Table 1; Supplementary Fig. 7). TBC47 compounds contain a pyrazolo[1,5-*a*]pyrimidine core, and more than 40 analogs were commercially available. Members of this chemotype were previously identified as potent whole-cell anti-TB hits in phenotypic screening and chemoinformatic studies,[49–51] but their antimycobacterial mechanism had not been defined. In our assays, four TBC47 analogs thermally destabilized MtbFtsZ and inhibited its GTPase activity. The series also showed evidence of cellular target engagement, with partial *ftsZ*-KD (2 ng/mL ATc) in GH161 reducing MIC50 values by 2- to 3-fold. Orthogonal assays further supported FtsZ modulation: DLS indicated that TBC47a completely blocked MtbFtsZ polymerization in vitro, whereas the closely related analog TBC47c appeared only to delay the depolymerization. Consistently, TBC47a disrupted Z-ring formation in cells, with loss of the normal mid-cell slit and diffuse distribution of MtbFtsZ-GFP (Fig. 2d).

Notably, the TBC47s and several other confirmed MtbFtsZ inhibitors showed considerable cytotoxicity in Vero E6 cells (Supplementary Table 2). To assess potential off-target activity against mammalian tubulin, we tested TBC47a and GDI-8134 (Fig. 2) in a tubulin polymerization assay (Supplementary Fig. 8). TBC47a slightly delayed tubulin polymerization, whereas GDI-8134 had little effect, although the final tubulin polymer size appeared similar under both conditions. These results suggest that TBC47a's cytotoxicity may partly reflect weak inhibition of mammalian tubulin. Overall, we validated more than 12 scaffolds (Fig. 2c) as novel MtbFtsZ inhibitors that disrupt mycobacterial cell division. We can further prioritize these hits based on cytotoxicity and counter-assay results.

BCP clustering of the MtbFtsZ-targeting inhibitors

To query whether the putative MtbFtsZ-targeting compounds disrupt mycobacterial growth via similar mechanisms of action, we modified our recently established BCP protocol to include a two-stage fluorescent D-amino acid (FDAA) staining procedure.[52] In brief, exponentially growing wild-type *M. bovis* BCG cells were pulse-stained with a cyan-colored FDAA (7-hydroxycoumarincarbonylamino-D-alanine, HADA), then exposed to titrating concentrations of compounds and allowed to grow for 48 hours. The second green-colored FDAA (3-[(7-Nitro-2,1,3-benzoxadiazol-4-yl)amino]-D-alanine, NADA) was then added directly to the bacterial cultures 24 hours before sample fixation (Fig. 3a). Fixed samples were chemically de-clumped using our recently established method[52] and subjected to high-throughput microscopy imaging and single-bacterium data analysis. Using rifampicin (RIF) as a bactericidal surrogate, we found that RIF treatment substantially dampened cell wall synthesis activity (loss of NADA signal), inhibited cell growth (retainment of HADA signal), and caused the cells to swell (cell width) in a concentration-dependent manner (Fig. 3b). By contrast, cell length did not change monotonically and was the longest at near-MIC concentrations (Fig. 3b). These observations were consistent with previous reports of RIF or *rpoB*-KD induced cytological changes, suggesting that our revised BCP methods could effectively capture dose-dependent growth and bacterial killing dynamics. TBC47a, a putative MtbFtsZ destabilizer, manifested a similar BCP profile, although the swelling phenotype was more pronounced than RIF (Fig. 3c). We also queried GH161 induced at different ATc concentrations and observed clear

dose-dependent cell-length variations (Supplementary Fig. 9). Notably, FtsZ knockdown had a negligible impact on cell width and NADA and HADA staining, implying that while cells underwent a profound morphological transformation, they remained alive and metabolically active.

The clear differences in concentration-dependent cytological dynamics between induced GH161 and the two example compounds suggested that dose-response trajectories convey salient information about compound MoAs in addition to per-dose comparisons. After batch normalization and feature selection (Methods), we projected the per-dose compound BCP data on a two-dimensional Uniform Manifold Approximation and Projection (UMAP) embedding. We observed a clear dose-dependent counterclockwise global organization on the UMAP embedding (Supplementary Fig. 10a). As expected, the UMAP embedding is structured by cell morphology and staining dynamics and compound MoAs (Supplementary Fig. 10c-d). To minimize noise from low-dose groups, which clustered into a compact cluster on the UMAP (Supplementary Fig. 10d), we took the Euclidean centroid of the low-dose cluster and used it as the consensus starting point for trajectory analysis. As illustrated in Fig. 3d, while inhibitors of DNA replication (e.g., moxifloxacin), translation (e.g., amikacin), and transcription (RIF) all followed a counterclockwise global trajectory, their endpoints (supra-MIC concentrations) differed significantly. By contrast, cell wall synthesis inhibition (e.g. isoniazid treatment) and *ftsZ*-KD induced abrupt and distinctive changes in their cellular phenotypes. Our selected panel (Table 1) of the confirmed FtsZ hits manifested varied trajectories, implying drastic differences in their MoAs.

We hypothesized that differences in dose-response trajectories may relate to the biochemical properties of these compounds. A major difference lies in their effects on FtsZ thermal stability, as revealed by the TSA assay (Table 1). By color-coding the dose-response trajectories of compounds with positive (stabilizer) and negative (destabilizer) TSA ΔT_m measures, we found, to our surprise, that stabilizers and destabilizer are separately clustered on the UMAP embedding and manifest distinct trajectories (Fig. 3e). A closer examination of their trajectory endpoints suggested that destabilizers exert strong inhibition on cell growth (higher HADA retainment) and activity (lower NADA signal) (Supplementary Fig. 10b). This hypothesis was further confirmed by comparing the dose-dependent NADA staining profiles across a panel of destabilizer and stabilizer compounds, whereby high-dose destabilizers manifested substantially stronger NADA staining inhibition compared to stabilizers (Fig. 3f).

GDI-8134 and GAC15 are the representative destabilizing and stabilizing compounds, respectively. They are two novel anti-TB compounds originally identified in a phenotypic screening of in-house HTS libraries. The anti-TB MICs are in the single-digit micromolar range, and the selectivity indices (SI, CC50 over H37Rv MIC) are reasonably good (Table 1). The physicochemical properties of the two bioactives conform to Lipinski's Rule of Five for oral drugs. Next, we set out to improve the potency and selectivity of the two validated hits through exploratory synthesis, inferring the structure-activity relationships (SARs).

Optimization and evaluation of GDI-8134 series

The screening hit GDI-8134 (Fig. 2c) contains a metabolically labile aliphatic linker. We first cyclized the linker while maintaining the overall chain length, thereby identifying GDI-8434. Optimization focused on the four parts of GDI-8434: the tetrahydroimidazopyridine and *tert*-butyl groups, the ethyl linker, and substitutions on the phenyl ring (SAR summary in Supplementary Fig. 11). A disubstituted analog GDI-8838 (Supplementary Fig. 12) is the best analog of the series (Fig. 4a). Although GDI-8838 did not show significant improvement in the MIC relative to GDI-8434, it exhibited reduced cytotoxicity (CC50 ~ 45 μM) and a twofold improvement in the SI. Replacing the methyl group with chlorine in GDI-8838 yielded GDI-8937, which has the lowest GTPase-inhibition IC_{50} at 14 μM, but its MIC was higher than that of GDI-8434.

GDI-8434 appeared to delay MtbFtsZ depolymerization in the DLS assay (Fig. 4b). It also showed strong cellular target engagement, producing one of the largest MIC50 shifts in the *ftsZ*-KD assay (Fig. 4c). To map the structural perturbations induced by GDI-8434 at the peptide level, we performed hydrogen-deuterium exchange mass spectrometry (HDX-MS) analysis (Fig. 4d). Following GDI-8434 treatment, significant reductions in deuterium incorporation were detected in three discrete peptide regions of MtbFtsZ, corresponding to residues 136–151, 159–176, and 345–362 (Supplementary Fig. 13a). The decreased exchange indicates that GDI-8434 binding reduces solvent accessibility and triggers pronounced conformational compaction in the corresponding FtsZ domains. Notably, the two centrally protected regions in the NTD are spatially distinct from the canonical GTP-binding pocket. In contrast, three other peptide segments spanning residues 89–95, 186–197, and 250–258 exhibited markedly elevated deuterium incorporation upon exposure to GDI-8434, suggesting local structural loosening and increased conformational flexibility in these regions. The deuterium uptake of these peptides in a GTPγS treatment was either unchanged or decreased. In the GTPase assay, a GDI-8434 analog behaved as a noncompetitive inhibitor, with its IC_{50} value remaining unchanged across increasing GTP concentrations, whereas the IC_{50} increased when assayed with the substrate-competitive inhibitor GTPγS (Supplementary Fig. 13b). Although these data support an allosteric mode of action of GDI-8434, the precise binding site and pose remain to be determined. In the BCP analysis (Fig. 3e), despite its distinct scaffold, GDI-8434 clustered with other confirmed thermal destabilizers, such as TBC47 and GDI-B029, suggesting that these compounds produce similar downstream effects on the mycobacterial divisome after engaging FtsZ in the cells.

GDI-8434 and GDI-8838 were further evaluated in pharmacological profiling (Fig. 4e; Supplementary Fig. 12). Both exhibited manageable plasma protein binding, moderate-to-high metabolic stability, and favorable solubility. In a kill-kinetics analysis (Fig. 4f), GDI-8434 reduced Mtb CFU by ~ 3 log10 at 10× MIC within about 7 days. The observed activity suggests the BCP, assayed at sub-inhibitory concentrations of FtsZ compound, could be used to identify and prioritize bactericidal agents. This killing profile is also consistent with reports of potent FtsZ inhibitors or clinical candidates active against other bacterial pathogens.[53,54] However, despite its attractive property profile, GDI-8838 lacked sufficient potency and selectivity to qualify as an anti-TB lead.

Evaluation and exploration of GAC15 with learning of cellular mechanism

GAC15, registered in PubChem as N-(3-chlorophenyl)-5-nitrothiophene-3-carboxamide (CID 154619), was a confirmed MtbFtsZ hit with an MIC as low as 1.4 μM and over 50-fold selectivity (Table 1). It stabilized MtbFtsZ in the TSA (Supplementary Fig. 14a) but did not inhibit its GTPase activity. It weakly delayed MtbFtsZ depolymerization in the DLS assay (Supplementary Fig. 14b). Regarding the structure and potency, GAC15 differs significantly from the 5-nitrothiophenes previously studied for their intracellular metabolism in Mtb[55] or *Staphylococcus*.[56] We investigated the mechanism of GAC15 in BCG, which possesses a nitroreduction system comparable to that of Mtb.[57,58]

First, microscopy confirmed that GAC15 disrupted the Z-ring morphology in *M. smegmatis* (Msmeg); the labelled FtsZ protein diffused over the cell within hours after GAC15 treatment (Fig. 5a). GAC15 also elongated *M. bovis* BCG WT cells at the MIC ~ 5 μM (Fig. 5b). As Msmeg normally cannot metabolize the nitroaromatic drug pretomanid and 5-nitrothiophene to produce sufficient nitric oxide (NO),[55,59] the GAC15 phenotypes could be attributed to FtsZ perturbation rather than to NO-mediated toxicity in this bacterium. To assess whether GAC15 undergoes deazaflavin (F_{420})-dependent nitroreduction in BCG, we quantified nitrite (NO_2^-) in treated cultures using the Griess assay, with pretomanid as a positive control. Whereas pretomanid produced a noticeable increase in NO_2^-, GAC15 barely increased nitrite production above the DMSO control (Fig. 5b). The nitro group could also be reduced by a mycothiol-dependent nitroreductase.[60,61] In this case, a GAC15 derivative would have an amino replacing the nitro group, while no nitrite is released.

Next, we isolated GAC15-resistant BCG mutants and estimated the resistance frequency at $> 1 \times 10^{-7}$. All nine mutants raised showed a 40-60-fold increase in GAC15 MIC but remained similarly susceptible to pretomanid (Supplementary Table 3). Whole-genome sequencing of six mutants identified insertions at different positions in a gene identical to *Rv2888c*, which encodes a nonessential 473-amino-acid amidase termed AmiC in Mtb (Fig. 5c), and an additional missense mutation in another nonessential gene (*Rv2048c* homolog) in one mutant. We analyzed the BCP of mutant GAC15-M1, which contains only a single insertion that changes and truncates the C-terminal region of AmiC. GAC15-M1 showed no obvious morphological difference from wild-type in the BCP. Based on a previous report implicating AmiC in intramycobacterial metabolism of small molecules,[62] GAC15 resistance may result from hydrolysis of the compound rather than an altered divisome.

On the other hand, we synthesized a small set of GAC15 analogs containing electron-withdrawing or electron-donating substituents, including the amino analog GAC15-14 and the des-nitro analog GAC15-11 (Fig. 5d). Replacing or removing the nitro group substantially reduced in vitro and cellular activity. A bromo analog GAC15-15 retained moderate anti-TB activity, whereas other modifications of the rings, such as dichlorination of aniline, generally decreased potency. BCP revealed that GAC15-15 treated WT cells closely resembled the GH161 cells induced for *ftsZ*-KD (Fig. S10). The antibacterial activity of

GAC15 or GAC15-15 was consistent with an on-target mechanism, exhibiting a large MIC50 shift in the *ftsZ*-KD-induced cells (Fig. 5e). Thus, the nitro group of GAC15 is important for FtsZ binding and antibacterial activity, but the nitro-reduced analogs are less active.

To learn the cellular metabolites, we performed a metabolic analysis by LC–MS/MS using the synthesized analogs and commercial compounds as standards (Fig. 5f, g; Supplementary Fig. 15). After BCG culture was exposed to 20 μM GAC15 for 24 h, only ~ 0.02% of the initial compound remained detectable in cell lysates or culture medium. While *m*-chloroaniline (CA) was a major metabolite at micromolar levels, supporting GAC15 hydrolysis as the main inactivation mechanism, NTC was not detected under multiple MS settings, likely because of its insufficient abundance and elusiveness. Furthermore, two nitro-reduced metabolites, GAC15-11 and GAC15-14, were detected at appreciable levels inside and outside cells, suggesting that reduction of the nitro group through F_{420}- or mycothiol-dependent pathways also occurred. Although NTC, its methyl ester, and CA showed limited whole-cell activity against BCG and Mtb, with MICs at 25–60 μM, GAC15-derived intracellular metabolites including NTC, GAC15-11 and − 14 could still bind to MtbFtsZ (Supplementary Fig. 14a; Fig. 5d), contributing to the potent antibacterial activity. Nonetheless, GAC15 and the dipeptide analogs are metabolically labile if not extensively modified and could be similarly compromised in other slowly growing mycobacteria.

Discussion

FtsZ is an attractive antimycobacterial target because it is an essential bacterial cytoskeletal protein that coordinates cell division and is sufficiently divergent from human tubulin to enable selective inhibition. Although FtsZ-directed discovery can be initiated through phenotypic screening, assigning antibacterial whole-cell activity to FtsZ requires complementary genetic, biochemical, and cellular evidence. Here, we first used CRISPRi knockdown to demonstrate the genetic vulnerability of FtsZ in BCG. Partial depletion of FtsZ resulted in a cell-elongation phenotype and sensitized the *ftsZ*-KD mutant GH161 to known MtbFtsZ inhibitors. An integrated workflow combining thermal-shift and GTPase assays, MIC50-shift measurements, cell morphology, protein polymerization and Z-ring analyses was implemented to screen and validate FtsZ-targeting compounds in mycobacteria. Screening ~ 5,000 whole-cell-active compounds identified multiple chemotypes that interacted with MtbFtsZ and could be broadly distinguished as thermal stabilizers or destabilizers. Orthogonal assays showed that these compounds perturbed FtsZ polymerization, depolymerization, Z-ring formation, or cellular localization, although individual compounds displayed different combinations of biochemical activity, cellular target engagement, cytotoxicity, and developability.

For hit prioritization and MoA inference, we leveraged Bacterial Cytological Profiling (BCP), which assumes specific physiological ties between compound MoAs and resultant cellular phenotypes.[63–66] Similar technology has been applied to identify tubulin modulators from mammalian cell-active compound collections.[67] Notably, however, our data and that of others imply that dose-responses are often non-monotonic at the cellular level, and we propose that dose-response cytological trajectories rather than single-dose cytological profiles are better predictors of compound MoAs. In this case, our

trajectory analysis effectively separates the FtsZ-directed compounds into two main clusters. Importantly, these two clusters reconcile with their corresponding TSA ΔT_m measures, suggesting that FtsZ-stabilizing and destabilizing compounds potentially inhibit mycobacterial growth via divergent mechanisms, with destabilizing compounds being substantially more bactericidal.

TBC47 and GDI-8434 are examples of destabilizing compounds with strong cellular and molecular evidence of FtsZ engagement, whereas GAC15 is a potent, selective stabilizer whose activity is limited by nitro-group dependence and poor metabolic stability. Overall, this work demonstrates that MtbFtsZ is chemically addressable and that mechanistically distinct FtsZ ligands can inhibit mycobacterial cell division. It also highlights the importance of integrating phenotypic and target-based approaches to distinguish genuine FtsZ-mediated antibacterial activity from compounds whose whole-cell effects arise through alternative mechanisms, thereby providing a framework for discovering anti-TB agents with novel mechanisms of action.

Phenotypic screening of pharmaceutical libraries against Mtb or related surrogate models has contributed to the discovery and approval of new anti-TB drugs and has generated extensive information on the molecular properties of thousands of antimycobacterial compounds.[68–71] However, many phenotypic hits lack target specificity and are associated with cytotoxicity or other liabilities that limit their progression. Target-based screening can provide complementary information and has produced several preclinical antibacterial candidates.[72] The TB Drug Accelerator (TBDA) consortium[73] has therefore developed approaches to prioritize targets that are both biologically vulnerable and amenable to development with a reasonable therapeutic rationale. FtsZ was identified as one such target, and we investigated it by screening a large collection of compounds with established whole-cell anti-TB activity.

Although the ten screening hits were confirmed to interact with and inhibit MtbFtsZ in vitro, we were unable to establish a structure-guided optimization program based on a co-crystal structure. This may reflect the conformational dynamics of MtbFtsZ, weak or transient ligand binding, or limited ligandability of the initial chemotypes. We therefore explored GDI-8134 and GAC15 based on microbiological profiling and pharmacological analysis, the approaches commonly used in a phenotypic program. Before extensive analog synthesis, both hits were evaluated in a panel of assays facilitated by TBDA member organizations to assess potential nonspecific antibacterial mechanisms and promiscuous membrane-associated activity.[74–76] Neither compound caused detectable DNA damage, membrane potential disruption, cell-wall stress, or ATP depletion at sub-MIC concentrations. Neither compound encountered cross-resistance in mycobacterial strains carrying mutations of common targets such as *inhA* and *mmpL3*. These results reduced, but did not completely exclude, the possibility that their cellular activity arose from mechanisms unrelated to FtsZ.

We completed hit assessment and biological evaluations of novel anti-TB compounds targeting FtsZ for cell-division inhibitors within a study period. The MtbFtsZ thermal destabilizers generally lack sufficient SAR space to improve potency and mitigate cytotoxicity. For the thermal stabilizer GAC15, the FtsZ-binding activity was strongly dependent on the 5-nitrothiophene moiety. The compound had little effect

on GTPase activity but delayed the depolymerization, suggesting a binding site distinct from the NTD–T7-loop catalytic interface. Whether GAC15 disrupts protein-protein interactions in the C-terminal region remains unsolved. FtsZ is estimated to be present at approximately 7,000–30,000 molecules per mycobacterial cell, depending on growth phase,[48] exceeding the abundance of RNA polymerase but far below that of ribosomes.[77] Although MtbFtsZ remains a druggable target in principle, the poor metabolic stability of GAC15 prevents adequate intracellular exposure to inhibit the cellular FtsZ pool.

Our strategy of screening the whole-cell active libraries differed from a binding site-centric approach,[78] and may have under-sampled compounds targeting an interdomain cleft (IDC) between the NTD and CTD of FtsZ and covered by the T7 loop. PC190723, the anti-staphylococcal FtsZ inhibitor, originated from a benzamide fragment and was developed through iterative rounds of synthetic chemistry.[24] Subsequent resistance mutant analysis and co-crystal structures established the IDC as a ligandable pocket.[53,79] However, the pocket varies substantially among bacterial species and genotypes.[80] Nonetheless, recent synthetic and computational studies have found new starting points for this site in various pathogens.[33,81–83] Defining the binding sites of MtbFtsZ thermal stabilizers identified in this study could therefore provide an alternative entry for future FtsZ drug discovery, although resistance liabilities will require careful assessment.

The workflow, particularly the validations, established here can also be applied to other FtsZ modalities, including microbial natural products, cyclic peptides, and BacPROTACs. In parallel, other mycobacterial divisome proteins, such as Wag31 and FtsW, may offer additional opportunities for developing cell-division inhibitors. Ultimately, successful hit progression will depend on achieving a balanced profile of antibacterial potency, selectivity, target engagement, resistance barrier, and physicochemical and pharmacokinetic properties.

Methods

Bacterial strains and culture conditions

M. tuberculosis H37Rv ATCC27294, *M. smegmatis* mc^{2}155 and *M. bovis* BCG str. Pasteur 1173P2 are from laboratory stock and were cultured in 7H9 (Becton-Dickinson, Franklin Lakes, NJ) Middlebrook medium supplemented with 10% oleic acid-albumin-dextrose-catalase (Becton-Dickinson, Franklin Lakes, NJ), 0.5% glycerol, and 0.05% tyloxapol or Tween 80 at 37°C. FtsZ CRISPRi strain of *M. bovis* BCG with kanamycin resistance marker was cultured with kanamycin at 20 mg/mL. *M. smegmatis* with FtsZ expression plasmid was cultured with kanamycin at 25 mg/mL.

Construction and confirmation of the CRISPRi ftsZ-knockdown strains

The CRISPRi plasmids targeting the non-template strand of the ftsZ genes were constructed following previously described methods[36,84]. Briefly, the sgRNA targeting the ftsZ sequences was cloned into the sgRNA scaffold of pJLR965 plasmid. Complementary oligonucleotides containing GGGA and AAAC

overhangs were synthesized, annealed and cloned into the BsmB1-digested pLJR965 backbone using T4 DNA ligase (400U/μl, NEB) at 20ºC for 30 min. The resulting ftsZ-targeting CRISPRi plasmid was transformed into the chemically competent DH5a cells. Transformants were selected on LB agar supplemented with 50 μg/ml kanamycin, and positive clones were validated through PCR and DNA sequencing.

The verified plasmids expressing CRISPRi sgRNA were subsequently electroporated into *M. bovis* BCG (Table S4). To determine the ATc concentration required for *ftsZ* knockdown, the constructed *ftsZ*-KD strains were exposed to a two-fold serial dilution of anhydrotetracycline (ATc), ranging from 200 to 0 ng/mL. Growth inhibition was determined following ATc induction at 37°C for 7 days. To confirm suppressed gene expression in the *ftsZ*-KD strain, GH161 was grown to an OD600 of 0.4–0.6, diluted to an OD600 of 0.002, and cultured in the presence of ATc at 0, 2, 3, 10, and 20 ng/mL for 5 days at 37°C, respectively. Total RNA of the ATc-induced strains was extracted as previously described,[85] and the transcriptional levels of *ftsZ* and its upstream and downstream genes were determined by quantitative reverse-transcription PCR (RT-qPCR) using gene-specific primers (Table S5).

MIC and MIC shifting assays with hit compounds

M. tuberculosis or *M. bovis* BCG strain was cultured to an optical density at 600 nm (OD_{600}) of 0.4–0.7. Compounds were added into 96-well plate by two-fold dilution from 200 μM in 100μL medium. Culture was diluted to OD_{600} of 0.002, which corresponded to 2 x 10^5 CFU/mL in this case, and seeded to each compound concentration in 100 μL medium per well. The final highest concentration of compounds was 100 μM and the final concentration of cells was 1 x 10^5 CFU/mL. The plate was incubated for 7 days at 37°C. MIC for each compound was determined using the resazurin reduction microplate assay (REMA).[86] Mixture of 20μL Alamar Blue (Thermo Fisher Scientific, Waltham, MA) and 12.5μL 20% tween-80 were added per well and incubated the plate for another 24h. The fluorescence signals of emission wavelength at 590 nm for each well were recorded, and MIC of H37Rv or BCG was defined as the lowest concentration where inhibition of fluorescence signal is greater than or equal to 90%. MIC was calculated by curve fitting the data of the relative growth versus drug concentration to a model named “log (inhibitor) versus normalized response – Variable slope” in GraphPad Prism 10.

The conditional mutant GH161 and the control strain expressing scrambled sgRNA were cultured in 7H9 with various concentrations of anhydrotetracycline induction (ATc = 0, 3, 5 ng/ml) in 96-well plates containing the twofold diluted compound and control wells. The plates were incubated at 37°C for 7 days and the relative growth curve of each sample was determined by Alamar Blue as described in previous paragraph. MIC 50 was defined as the lowest concentration where inhibition of fluorescence signal is greater than or equal to 50%. The MIC shift of the FtsZ-KD was calculated as the fold change between MIC 50 at ATc 0 ng/mL and MIC 50 at various concentrations of ATc.

Cloning, protein overexpression and purification

M. tuberculosis ftsZ gene (encoding residues 1–379), codon-optimized for expression in *E. coli*, was synthesized and cloned into the pET-28b vector containing an N-terminal 6xHis tag followed by a TEV protease cleavage site. The recombinant plasmid was transformed into *E. coli* BL21(DE3) cells. Protein expression was carried out in Terrific Broth medium at 18°C for 16 h in the presence of 0.5 mM IPTG.

Cells were harvested by centrifugation, resuspended in lysis buffer (25 mM Tris-HCl, pH 7.5, 500 mM NaCl, and 10% glycerol), and lysed by high-pressure homogenization. The lysate was clarified by centrifugation at 20,000 rpm for 35 min at 4°C, and the supernatant was applied to a 5 mL HisTrap HP column (Cytiva). After washing with wash buffer (25 mM Tris-HCl, pH 7.5, 500 mM NaCl, 10% glycerol, and 20 mM imidazole), the bound protein was eluted with lysis buffer containing 300 mM imidazole.

The eluted protein was incubated with TEV protease and dialyzed overnight against 2 liters of lysis buffer to remove the N-terminal 6xHis tag. The digestion mixture was subsequently passed through the HisTrap HP column, and the flow-through fraction containing tag-free FtsZ was collected. The protein was further purified by size-exclusion chromatography using a HiLoad 16/600 Superdex 200 prep-grade column (Cytiva) equilibrated with gel-filtration buffer consisting of 25 mM HEPES (pH 7.5), 50 mM KCl, 0.1 mM EDTA, 1 mM DTT, and 10% glycerol. Protein purity was verified by SDS–PAGE. Purified FtsZ was concentrated to 16 mg/mL, flash-frozen in liquid nitrogen, and stored at − 80°C until use.

Thermal Shift Assay (TSA)

TSA was used to detect protein-compound interactions and performed in a 384-well microliter plate with the Applied Biosystems QuantStudio 7 Real-Time PCR system (Thermo Fisher Scientific, Waltham, MA). The reactions contained 5 μM FtsZ protein, 200uM GDP and 10X SYPRO Orange in 10 μL MES buffer (50 mM MES, pH6.5, 50 mM potassium acetate, 5 mM magnesium acetate). Each compound was incubated with FtsZ protein and GDP at room temperature for 2h or 16h, before adding 10X SYPRO Orange. Melting curves were obtained by gradually increasing the temperature from 25°C to 99°C (0.05°C per second), with fluorescence intensities read at each temperature using optical filters set for the carboxyrhodamine (ROX) dye. Melting temperatures (T_m values) were calculated using the Protein Thermal Shift software.

Determination of FtsZ GTPase and IC_{50}

FtsZ GTPase activity was measured using a malachite green assay to quantify inorganic phosphate release. Briefly, purified FtsZ protein (4 μM) was preincubated with the test compound in the assay buffer containing 50 mM MES (pH 6.5), 100 mM KCl, and 5 mM $MgCl_2$ at room temperature for 2 hours. Reactions were initiated by adding GTP to a final concentration of 125 μM and incubated for an additional 3 hours. Reactions were then terminated by addition of malachite green reagent, and the amount of released inorganic phosphate was quantified by measuring absorbance at 620 nm using an EnVision plate reader (PerkinElmer, Waltham, MA, USA). Absorbance values were corrected by subtracting the background signal from the assay buffer control. IC50 was defined as the lowest concentration where inhibition of absorbance signal is greater than or equal to 50%.

Dynamic light scattering (DLS) assay

DLS measurement was performed to assess the dynamics of FtsZ polymerization and depolymerization driven by GTP hydrolysis. Samples containing 4 μM FtsZ and either 50 μM test compound or DMSO vehicle control were prepared in GTPase assay buffer and centrifuged before analysis to remove insoluble particles. Measurements were initiated immediately after the addition of GTP and collected at 25°C using a DynaPro Plate Reader III (Waters) equipped with an 830 nm laser. The average particle radius of GTP-stimulated FtsZ was calculated using the manufacturer-provided software DYNAMICS 8.3. FtsZ polymerization curves were plotted as particle radius versus time using GraphPad Prism 11.

Cell length measurement

Bacteria grew to an OD600 around 0.1 in the absence or presence of the candidate compounds at MIC concentration for 3 days. After treatment, the cells were harvested by centrifugation, washed in PBS, and fixed in 4% paraformaldehyde. Cell suspensions were mounted on agarose pads on glass slides and covered with coverslip. Bright-field images were acquired on a Nikon Eclipse Ti2 microscope equipped with a 100X Nikon Plan Fluor oil immersion objective and Nikon DS-Qi2 camera using NIS-Elements software. Images were analyzed using Fiji/ImageJ software and ObjectJ plugin.[87,88] When cell lengths were measured, around 100 cells from 2 independent biological replicates were analyzed. Statistical analyses were carried out with GraphPad Prism 10.

Bacterial Cytological Profiling

Sample preparation

M. bovis BCG str. Pasteur 1173P2 were grown to mid-exponential phase (OD_{600}~0.15) then stained with 25μM HADA (Aladdin, China. Cat. H287563) supplemented to plain 7H9 for one day. HADA-stained bacilli were then washed twice with equal volume of plain 7H9, then resuspended in 7H9 to a final density of OD_{600}~0.1. Serial 2-fold diluted compounds of interest as well as DMSO controls were prepared in 7H9 broth and mixed with an equal volume of stained bacterial suspension in flat-bottom 96 well plates. After 48 hours of standing incubation at 37℃, a second FDAA, NADA-green (GLPBIO, Cat. GC50534) was supplemented to a final concentration of 25 μM. After 24 hours of NADA staining, cells were fixed by adding one eighth volume of 16% PFA (OKA, China. Cat. GCDF0131) then incubated in the dark at room temperature for one hour. Fixed BCP samples were removed from the BSL-2 laboratory and stored at 4℃ before subsequent procedures.

At the day of imaging, 160μL of fixed bacilli were transferred to a non-skirted 0.2mL PCR plate. Cells were pelleted by centrifugation (3,000×g, 5min) and the supernatant removed carefully using a multichannel pipettor. Pellets were resuspended in a freshly mixed declumping solution (100 mM Tris-HCl, pH = 7.5, 1% m-xylene, 1% Triton X-100 [wt/vol]) modified from a recently established protocol.[52] Cells were collected by centrifugation (3,000×g, 5min), washed once with PBSTx (1×PBS, 0.1% TritonX-100), then resuspended in 1/10 volume of PBSTx.

Fluorescent microscopy

PBS-buffered agarose gel pads were prepared according to our previous work[52] with a few modifications: Nile red (Mreda, China. Cat. M057563, stored in pure ethanol) and Methyl green (Biotopped, China. Cat. M6020R, dissolved and stored in water) were added to melted agarose to 0.1μg/mL and 200 μM, respectively. Fluorescence microscopy was caried out on a motorized Nikon Ti-E inverted fluorescence microscope equipped with a 100× oil-immersion objective (Nikon, CFI Plan Apo DM Lambda MRD31905), a Dhyana 401D sCMOS camera (2048 × 2048 pixels, 16-bit; 6.5 μm pixel size), a Chroma Quad bandpass filter set (89402 ET – 391 – 32/479 – 33/554 – 24/638 – 31), and an Mshot MG120 multi-color LED lamp (Ex. centered near 385/460/550/625nm). Automated 5-channel (4 fluorescence channels and 1 phase contrast) imaging were performed using custom python scripts and 16 tiled imaging fields were collected for each BCP sample.

Microscopy image analysis

Phase-contrast and multi-channel fluorescence images of *M. bovis* BCG were segmented using Omnipose with the *bact_phase_omni* model.[89] Illumination bias was corrected with BaSiC[90] and channel drift was aligned via phase cross-correlation. Single-cell morphological and fluorescence features were extracted using MOMIA2,[52] including cell dimensions, curvature, Hu moments, and 32-dimensional InShaDe shape descriptors.[91] Fluorescence intensities from four channels were $\log_2$-transformed and summarized as mean, median, quartiles, CV, skewness, and kurtosis. Features were batch-normalized by Z-score transformation using intra-batch vehicle controls as reference. Samples were aggregated by computing population-level statistics (mean, median, IQR, CV, skewness, Q1, Q3) and visualized via UMAP embedding. Detailed analyses are provided as Jupyter notebooks available at https://github.com/jzrolling/ftsZ_bcp.

Mutant isolation

Serial passage was used for resistant mutant isolation of anti-FtsZ hit compounds. Briefly, *M. bovis* BCG was cultured to OD*600* 0.4–0.7 as described before. The culture was diluted to OD*600* 0.1 in 5 mL 7H9 with hit compound at MIC concentration and further incubated for 7 days at 37°C. The cells were collected by centrifuge 5000 x g for 10 min and resuspended in 5 mL 7H9 to OD*600* 0.1 with 2xMIC compound. Concentration increased by 1xMIC in every round of inoculation and the process continues for up to 5xMIC. Single colonies of resistant mutant were selected by plating 50 μL bacteria from liquid medium on 7H10 agar plates with compound at 5xMIC concentration. Expect GAC15, no colonies growing on the selective plate of anti-FtsZ hit compounds after twice serial passage. The resistance colonies of GAC15 were confirmed by MIC determination. The nucleotide variations of GAC15 mutant strains were identified by whole genome sequencing.

Hydrogen-Deuterium Exchange Mass Spectrometry

A stock solution of FtsZ (1 mg/mL) and small molecules were mixed in 50 μL buffer (25 mM HEPES, 50 mM KCl, 0.1 mM EDTA, 1 mM DTT, 2.5% DMSO, pH 7.4) at a molar ratio of FtsZ to small molecule of approximately 1:100. The protein mixture was diluted 20-fold with deuteroxide, and the resulting solution

was incubated at 4°C. The deuteration process was monitored at 5 s, 15 s, 1 min, 10 min, 30 min, 60 min and 240 min, and 50 μL of protein solution was taken and quenched by adding 50 μL of 200 mM pH 1.8 phosphate buffer with 200 mM Gn·HCl and 200 mM DTT, which was pre-cooled to 0°C. Pepsin digestion was carried out by automatic loading of 5 μL protein sample onto Waters Enzymate online pepsin column, and the data of hydrogen-deuterium exchange mass spectrometry were collected by using Waters SYNAPT G2-S2i mass spectrometry. Waters PLGS global server 2.3 was utilized to identify the peptide fingerprint of enzymatically hydrolyzed fragments, and Waters DynamX was employed to plot the curve of the deuterium number of each fragment over time. Peptide regions found to have altered mass after binding were then selected to describe the dynamic deuteration process.

Griess assay measuring NO_2^- in the growth culture

The assay followed a published protocol[92]. Briefly, a nitrite calibration curve was generated by measuring the absorbance at 548 nm of nitrite standards using the Griess Reagent Kit (Invitrogen™, Thermo Fisher Scientific, Waltham, MA, USA). Bacteria were cultured to an OD600 of approximately 0.3 and then treated with the test compounds at 20 μM. At each time point, the supernatant of culture (200 μL) was transferred to a 96-well plate and mixed with 20 μL of Griess reagent. After incubation for 30 min at room temperature, the absorbance at 548 nm was measured. Nitrite concentrations were calculated from the calibration curve.

Analysis of GAC15 metabolites by LC-MS/MS

Bacteria were cultured to an OD600 of approximately 0.4–0.8 and harvested by centrifugation. The cells were resuspended to a high-density bacterial suspension (OD600 ≈ 4.0) in 7H9 medium and incubated with 20 μM test compound for 24 h at 37°C. At the termination, 1 mL of the bacterial culture was rapidly chilled on ice, and the cells were washed three times with precooled phosphate-buffered saline (PBS) containing 0.05% Tween 80 and 2% DMSO. The cell pellet was then resuspended in 100 μL of precooled PBS and mixed with 400 μL of extraction solvent (acetonitrile:methanol:water, 40:40:20, v/v/v). Cells were disrupted using a Precellys Evolution Touch homogenizer (hard mode, 7200 rpm, shaking for 40 s, cooling on ice for 3 min, repeated for 6 cycles), with the entire process maintained on ice or at low temperature. Lysate was kept at 4°C overnight and subsequently centrifuged at 18,000 × g for 30 min at 4°C to obtain the supernatant as a lysate sample. The cleared cell-free medium was mixed with 4-fold volume of the extraction solvent to produce a sample for MS.

For quantitative analysis, a calibration curve was constructed using a standard compound over the concentration range of 2–2000 nM in a blank buffer consisting of blank growth medium 7H9 mixed with extraction solvent (1:4). Aliquots (150 μL) of medium sample, lysate sample, and calibration standards were transferred into a 96-well plate. 100 μL of 80% acetonitrile in water, containing 300 ng/ml labetalol for positive ionization or 1000 ng/ml tolbutamide for negative ionization as the internal standard, was added to the wells, and the plate was mixed by shaking. The samples were then analyzed by LC-MS/MS in Multiple Reaction Monitoring (MRM) mode.

LC-MS/MS was performed on a TSQ Quantum triple quadrupole mass spectrometer (Thermo Fisher Scientific) and a UPLC system (Waters) equipped with a Kinetex 1.7 μm C18 column (30 × 2.1 mm, Phenomenex) for quantitative analysis. The mobile phase consisted of 100% water with 0.1% formic acid (solvent A) and 100% acetonitrile with 0.1% formic acid (solvent B), at a flow rate of 0.6 mL/min. The gradient was 0.50 min, 90% A: 10% B; 1.00 min, 5% A: 95% B;1.50 min, 5% A: 95% B; 1.52 min, 90% A: 10% B; 2.00 min, 90% A: 10% B.

Declarations

Data Availability

Previously published crystal structure 1RLU[12] was downloaded from the Protein Data Bank (www.wwpdb.org). Bacterial Cytological Profiling analyses are provided as Jupyter notebooks available at https://github.com/jzrolling/ftsZ_bcp.

Founding Sources

This work is supported by the Gates Foundation grant xxx-xxxxx (GHDDI) and grant xxx-xxxx (T.P.), and J.Z. discloses support for the research of this work from the Strategic Priority Research Program of the Chinese Academy of Sciences (XDB0810000).

Competing Interests

The authors declare no competing interests related to the contents of this manuscript.

Author Contributions

Conceptualization: S.C. and J.Z.; Investigation: J.W., Q.H., L.X., T.P., J.Z., and S.C.; Data curation: J.W., Q.H., H.W. G.X., H.J., Y.X., Y.C., M.P., M.Z., L.Z,, E.L., Y.Z. and RY.L.; Formal analysis: J.W, Q.H., L.X., Z.Z., T.P., J.Z. and S.C.; Methodology: J.W, Q.H, H.W. G.X., H.J, Y.X., Z.Z., J.Z.R and S.C.; Resources: C.C., R.Z., J.G., Y.L. and T.P.; Validation: J.G., RH.L and Y.L.; Visualization: J.W., H.J., J.Z. and S.C.; Writing−original draft: J.W., Q.H, H.W., G.X., H.J., J.Z. and S.C.; Writing−review & editing: all authors; Supervision: J.Z and S.C.; Funding Acquisition: R.Z., T.P., and J.Z. All authors have approved the final version of the manuscript

Acknowledgements

We thank GSK Spain, TB Alliance, and Medicines for Malarial Venture (MMV) for providing compound libraries for the screening.

References

1. Den Blaauwen T, Hamoen LW, Levin PA (2017) The divisome at 25: the road ahead. Curr Opin Microbiol 36:85–94
2. Cameron TA, Margolin W (2024) Insights into the assembly and regulation of the bacterial divisome. Nat Rev Microbiol 22:33–45
3. Egan AJF, Vollmer W (2015) The stoichiometric divisome: a hypothesis. Front Microbiol 6
4. Mahone CR, Goley ED (2020) Bacterial cell division at a glance. J Cell Sci 133:jcs237057
5. Adams DW, Errington J (2009) Bacterial cell division: assembly, maintenance and disassembly of the Z ring. Nat Rev Microbiol 7:642–653
6. Bi EF, Lutkenhaus J (1991) FtsZ ring structure associated with division in *Escherichia coli*. Natrue 354:161–164
7. Du S, Lutkenhaus J (2019) At the Heart of Bacterial Cytokinesis: The Z Ring. Trends Microbiol 27:781–791
8. Bisson-Filho AW et al (2017) Treadmilling by FtsZ filaments drives peptidoglycan synthesis and bacterial cell division. Science 355:739–743
9. Yang X et al (2017) GTPase activity–coupled treadmilling of the bacterial tubulin FtsZ organizes septal cell wall synthesis. Science 355:744–747
10. Battaje RR, Piyush R, Pratap V, Panda D (2023) Models versus pathogens: how conserved is the FtsZ in bacteria? Biosci Rep 43:BSR20221664
11. Hurley KA et al (2016) Targeting the Bacterial Division Protein FtsZ. J Med Chem 59:6975–6998
12. Leung AKW et al (2004) Structure of Mycobacterium tuberculosis FtsZ reveals unexpected, G protein-like conformational switches. J Mol Biol 342:953–970
13. Wagstaff JM et al (2017) A Polymerization-Associated Structural Switch in FtsZ That Enables Treadmilling of Model Filaments. mBio 8:e00254–e00217
14. Fujita J et al (2023) Structures of a FtsZ single protofilament and a double-helical tube in complex with a monobody. Nat Commun 14:4073
15. Du S, Park K, Lutkenhaus J (2015) Oligomerization of FtsZ converts the FtsZ tail motif (conserved carboxy-terminal peptide) into a multivalent ligand with high avidity for partners ZipA and SlmA. Mol Microbiol 95:173–188
16. Duman R et al (2013) Structural and genetic analyses reveal the protein SepF as a new membrane anchor for the Z ring. *Proc. Natl. Acad. Sci.* 110
17. Buske PJ, Levin PA, Extreme C (2012) Terminus of Bacterial Cytoskeletal Protein FtsZ Plays Fundamental Role in Assembly Independent of Modulatory Proteins. J Biol Chem 287:10945–10957
18. Li Y et al (2025) ZapC crosslinks FtsZ filaments through a dual-binding mechanism modulated by the intrinsically disordered linker of FtsZ in *Escherichia coli*. mBio 16:e02622–e02625

19. Guan F et al (2018) Lateral interactions between protofilaments of the bacterial tubulin homolog FtsZ are essential for cell division. eLife 7:e35578
20. Straniero V et al (2020) Benzamide Derivatives Targeting the Cell Division Protein FtsZ: Modifications of the Linker and the Benzodioxane Scaffold and Their Effects on Antimicrobial Activity. Antibiotics 9:160
21. Kusuma KD, Payne M, Ung AT, Bottomley AL, Harry E (2019) J. FtsZ as an Antibacterial Target: Status and Guidelines for Progressing This Avenue. ACS Infect Dis 5:1279–1294
22. Andreu JM, Huecas S, Araújo-Bazán L, Vázquez-Villa H, Martín-Fontecha M (2022) The Search for Antibacterial Inhibitors Targeting Cell Division Protein FtsZ at Its Nucleotide and Allosteric Binding Sites. Biomedicines 10:1825
23. den Blaauwen T, Andreu JM, Monasterio O (2014) Bacterial cell division proteins as antibiotic targets. Bioorg Chem 55:27–38
24. Haydon DJ et al (2008) An Inhibitor of FtsZ with Potent and Selective Anti-Staphylococcal Activity. Science 321:1673–1675
25. Kaul M et al (2015) TXA709, an FtsZ-Targeting Benzamide Prodrug with Improved Pharmacokinetics and Enhanced *In Vivo* Efficacy against Methicillin-Resistant *Staphylococcus aureus*. Antimicrob Agents Chemother 59:4845–4855
26. Baranowski C, Rego EH, Rubin EJ (2019) The Dream of a Mycobacterium. Microbiol Spectr 7, 7.2.38
27. Meyer FM, Bramkamp M (2024) Cell wall synthesizing complexes in *Mycobacteriales*. Curr Opin Microbiol 79:102478
28. White EL, Suling WJ, Larry J, Ross LES, Robert C (2002) Reynolds. 2-Alkoxycarbonylaminopyridines: inhibitors of *Mycobacterium tuberculosis* FtsZ. J Antimicrob Chemother 50:111–114
29. Margalit DN et al (2004) Targeting cell division: Small-molecule inhibitors of FtsZ GTPase perturb cytokinetic ring assembly and induce bacterial lethality. *Proc. Natl. Acad. Sci.* 101, 11821–11826
30. Huang Q et al (2006) Targeting FtsZ for Antituberculosis Drug Discovery: Noncytotoxic Taxanes as Novel Antituberculosis Agents. J Med Chem 49:463–466
31. Chen Y, Anderson DE, Rajagopalan M, Erickson HP (2007) Assembly Dynamics of *Mycobacterium tuberculosis* FtsZ. J Biol Chem 282:27736–27743
32. Mathew B et al (2016) Screening and Development of New Inhibitors of FtsZ from *M. Tuberculosis*. PLoS ONE 11:e0164100
33. Straniero V et al (2016) 3-(Benzodioxan-2-ylmethoxy)-2,6-difluorobenzamides bearing hydrophobic substituents at the 7-position of the benzodioxane nucleus potently inhibit methicillin-resistant Sa and Mtb cell division. Eur J Med Chem 120:227–243
34. Bhondwe P, Sengar N, Bodiwala HS, Singh IP, Panda D (2024) An adamantyl-caffeoyl-anilide exhibits broad-spectrum antibacterial activity by inhibiting FtsZ assembly and Z-ring formation. Int J Biol Macromol 259:129255

35. Zhang M et al (2025) Microbiological evidence for the trisubstituted benzimidazoles targeting MmpL3 in *Mycobacterium tuberculosis*. Antimicrob Agents Chemother 69:e00368–e00325
36. Rock JM et al (2017) Programmable transcriptional repression in mycobacteria using an orthogonal CRISPR interference platform. Nat Microbiol 2:16274
37. Li S et al (2022) CRISPRi chemical genetics and comparative genomics identify genes mediating drug potency in *Mycobacterium tuberculosis*. Nat Microbiol 7:766–779
38. Singh D et al (2014) SB-RA-2001 Inhibits Bacterial Proliferation by Targeting FtsZ Assembly. Biochemistry 53:2979–2992
39. Llowarch P, Usselmann L, Ivanov D, Holdgate GA (2023) Thermal unfolding methods in drug discovery. Biophys Rev 4:021305
40. Gao K, Oerlemans R, Groves MR (2020) Theory and applications of differential scanning fluorimetry in early-stage drug discovery. Biophys Rev 12:85–104
41. Niesen FH, Berglund H, Vedadi M (2007) The use of differential scanning fluorimetry to detect ligand interactions that promote protein stability. Nat Protoc 2:2212–2221
42. Goldman C R. Target Discovery for New Antitubercular Drugs Using a Large Dataset of Growth Inhibitors from PubChem. Infect Disord - Drug Targets 20, 352–366
43. Ballell L et al (2013) Fueling Open-Source Drug Discovery: 177 Small-Molecule Leads against *Tuberculosis*. ChemMedChem 8:313–321
44. Samby K et al (2022) The Pandemic Response BoxAccelerating Drug Discovery Efforts after Disease Outbreaks. ACS Infect Dis 8:713–720
45. Ramos-León F et al (2021) A conserved cell division protein directly regulates FtsZ dynamics in filamentous and unicellular actinobacteria. *eLife* 10, e63387
46. Panevska A, Šakanović A, Paccione G, Rivas G, Schwille P (2026) Optimizing spatial organization of FtsZ rings for large-scale constriction in synthetic cells. Nat Commun 17:2320
47. Dziadek J, Rutherford SA, Madiraju MV, Atkinson MAL, Rajagopalan M (2003) Conditional expression of *Mycobacterium smegmatis ftsZ*, an essential cell division gene. Microbiology 149:1593–1603
48. Dziadek J, Madiraju MVVS, Rutherford SA, Atkinson MAL, Rajagopalan M (2002) Physiological consequences associated with overproduction of *Mycobacterium tuberculosis* FtsZ in mycobacterial hosts. Microbiology 148:961–971
49. Maddry JA et al (2009) Antituberculosis activity of the molecular libraries screening center network library. Tuberculosis 89:354–363
50. Reynolds RC et al (2012) High throughput screening of a library based on kinase inhibitor scaffolds against *Mycobacterium tuberculosis* H37Rv. Tuberculosis 92:72–83
51. Ekins S et al (2013) Bayesian Models Leveraging Bioactivity and Cytotoxicity Information for Drug Discovery. Chem Biol 20:370–378
52. Liu Q et al (2025) High-throughput cytological profiling uncovers genotype-phenotype associations in *Mycobacterium tuberculosis* clinical isolates. *mSystems* 10, e00972-25

53. Bryan E et al (2023) Structural and Antibacterial Characterization of a New Benzamide FtsZ Inhibitor with Superior Bactericidal Activity and In Vivo Efficacy Against Multidrug-Resistant *Staphylococcus aureus*. ACS Chem Biol 18:629–642
54. Scoffone VC et al (2022) Bactericidal and Anti-Biofilm Activity of the FtsZ Inhibitor C109 against *Acinetobacter baumannii*. Antibiotics 11:1571
55. Hartkoorn RC et al (2014) Mechanism of Action of 5-Nitrothiophenes against *Mycobacterium tuberculosis*. Antimicrob Agents Chemother 58:2944–2947
56. Patel JS et al (2021) Bayesian Modeling and Intrabacterial Drug Metabolism Applied to Drug-Resistant *Staphylococcus aureus*. ACS Infect Dis 7:2508–2521
57. Choi K-P, Kendrick N, Daniels L (2002) Demonstration that *fbiC* Is Required by *Mycobacterium bovis* BCG for Coenzyme F_{420} and FO Biosynthesis. J Bacteriol 184:2420–2428
58. Eke IE, Abramovitch RB (2025) Functions of nitroreductases in mycobacterial physiology and drug susceptibility. J Bacteriol 207:e00326–e00324
59. Dogra M et al (2011) Comparative bioactivation of the novel anti-tuberculosis agent PA-824 in *Mycobacteria* and a subcellular fraction of human liver. Br J Pharmacol 162:226–236
60. Albesa-Jové D et al (2014) Rv2466c Mediates the Activation of TP053 To Kill Replicating and Non-replicating *Mycobacterium tuberculosis*. ACS Chem Biol 9:1567–1575
61. Negri A et al (2018) Identification of a Mycothiol-Dependent Nitroreductase from *Mycobacterium tuberculosis*. ACS Infect Dis 4:771–787
62. Libardo MDJ et al (2021) Resistance of Mycobacterium tuberculosis to indole 4-carboxamides occurs through alterations in drug metabolism and tryptophan biosynthesis. Cell Chem Biol 28:1180–1191e20
63. Nonejuie P, Burkart M, Pogliano K, Pogliano J (2013) Bacterial cytological profiling rapidly identifies the cellular pathways targeted by antibacterial molecules. *Proc. Natl. Acad. Sci.* 110, 16169–16174
64. De Wet TJ, Winkler KR, Mhlanga M, Mizrahi V, Warner DF (2020) Arrayed CRISPRi and quantitative imaging describe the morphotypic landscape of essential mycobacterial genes. *eLife* 9, e60083
65. Smith TC et al (2020) Morphological profiling of tubercle bacilli identifies drug pathways of action. *Proc. Natl. Acad. Sci.* 117, 18744–18753
66. Quach D et al (2025) Deep learning–driven bacterial cytological profiling to determine antimicrobial mechanisms in *Mycobacterium tuberculosis*. *Proc. Natl. Acad. Sci.* 122, e2419813122
67. Akbarzadeh M et al (2022) Morphological profiling by means of the Cell Painting assay enables identification of tubulin-targeting compounds. Cell Chem Biol 29:1053–1064e3
68. Chung GA, Aktar Z, Jackson S, Duncan K (1995) High-throughput screen for detecting antimycobacterial agents. Antimicrob Agents Chemother 39:2235–2238
69. Grzelak EM et al (2019) Strategies in anti-Mycobacterium tuberculosis drug discovery based on phenotypic screening. J Antibiot (Tokyo) 72:719–728
70. Abrahams KA, Besra GS (2020) Mycobacterial drug discovery. RSC Med Chem 11:1354–1365

71. Makarov V, Salina E, Reynolds RC, Zin K, P. P., Ekins S (2020) Molecule Property Analyses of Active Compounds for *Mycobacterium tuberculosis*. J Med Chem 63:8917–8955
72. Schnappinger D et al (2026) Integrating chemical, genetic, and feasibility assessments for anti-tubercular target validation. EMBO Mol Med 18:1495–1507
73. Briggs KL, Russell BJ, Warner P, Duncan K, Berthel SJ (2026) Building and managing a complex drug discovery consortium: insights from the tuberculosis drug accelerator. Drug Discov Today 31:104688
74. Ames L et al (2025) Common Biological Properties of *Mycobacterium tuberculosis* MmpL3 Inhibitors. ACS Infect Dis 11:2523–2533
75. Bond AN et al (2025) Reference-based chemical-genetic interaction profiling to elucidate small molecule mechanism of action in *Mycobacterium tuberculosis*. Nat Commun 16:9673
76. Eke IE, Williams JT, Abramovitch RB (2025) Genetic and Cheminformatic Characterization of *Mycobacterium tuberculosis* Inhibitors Discovered in the Molecular Libraries Small Molecule Repository. ACS Infect Dis 11:882–893
77. Bakshi S, Siryaporn A, Goulian M, Weisshaar JC (2012) Superresolution imaging of ribosomes and RNA polymerase in live Escherichia coli cells. Mol Microbiol 85:21–38
78. Casiraghi A, Suigo L, Valoti E, Straniero V (2020) Targeting Bacterial Cell Division: A Binding Site-Centered Approach to the Most Promising Inhibitors of the Essential Protein FtsZ. Antibiotics 9:69
79. Pradhan P, Margolin W, Beuria TK (2021) Targeting the Achilles Heel of FtsZ: The Interdomain Cleft. Front Microbiol 12:732796
80. Miguel A et al (2015) Variations in the Binding Pocket of an Inhibitor of the Bacterial Division Protein FtsZ across Genotypes and Species. PLOS Comput Biol 11:e1004117
81. Suigo L, Lanzini A, Straniero V, Margolin W (2026) Mechanistic Insights into the Antimicrobial Effect of Benzodioxane-Benzamides Against *Escherichia coli*. Antibiotics 15:126
82. Sciò P et al (2025) Identification of a New FtsZ Inhibitor by Virtual Screening, Mechanistic Insights, and Structure–Activity Relationship Analyses. ACS Infect Dis 11:998–1007
83. Rosado-Lugo JD et al (2022) Evaluation of 2,6-difluoro-3-(oxazol-2-ylmethoxy)benzamide chemotypes as Gram-negative FtsZ inhibitors. J Antibiot (Tokyo) 75:385–395
84. Wong AI, Rock JM (2021) CRISPR Interference (CRISPRi) for Targeted Gene Silencing in Mycobacteria. Mycobacteria Protocols, vol 2314. Humana, New York, NY, pp 343–364
85. Xiao G et al (2025) Identification of a phenyl ester covalent inhibitor of caseinolytic protease and analysis of the ClpP1P2 inhibition in mycobacteria. *mLife* 4, 155–168
86. Palomino J-C et al (2002) Resazurin Microtiter Assay Plate: Simple and Inexpensive Method for Detection of Drug Resistance in Mycobacterium tuberculosis. Antimicrob Agents Chemother 46:2720–2722
87. Schneider CA, Rasband WS, Eliceiri K (2012) W. NIH Image to ImageJ: 25 years of image analysis. Nat Methods 9:671–675

88. Vischer NOE et al (2015) Cell age dependent concentration of *Escherichia coli* divisome proteins analyzed with ImageJ and ObjectJ. Front Microbiol 6
89. Cutler KJ et al (2022) Omnipose: a high-precision morphology-independent solution for bacterial cell segmentation. Nat Methods 19:1438–1448
90. Peng T et al (2017) A BaSiC tool for background and shading correction of optical microscopy images. Nat Commun 8:14836
91. Al-Thelaya K et al (2021) InShaDe: Invariant Shape Descriptors for visual 2D and 3D cellular and nuclear shape analysis and classification. Comput Graph 98:105–125
92. Wang X et al (2020) Antitubercular Triazines: Optimization and Intrabacterial Metabolism. Cell Chem Biol 27:172–185e11

Table

Table 1 is available in the Supplementary Files section.

Figures

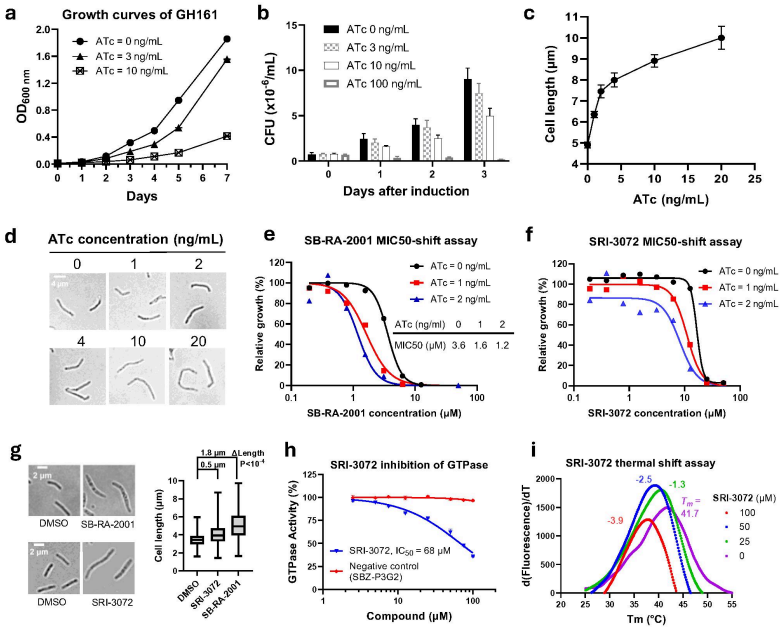


Figure 1. Characterization of the *ftsZ* CRISPRi knockdown (KD) strain GH161, and validation of two reported anti-TB FtsZ inhibitors. (**a**) Growth curves of GH161 over 7 days, induced by three concentrations of anhydrotetracycline (ATc) fed exogenously. (**b**) Assessment of the viability of GH161 by counting the colony-forming units (CFUs) on 7H10 agar plates after ATc induction. (**c**) Increased cell length in GH161 after ATc-induced *ftsZ*-KD for two days. The error bar shows the standard error of the mean (n = 99-203 cells). (**d**) Images of GH161 cells after the *ftsZ* KD. (**e**) MIC50-shift analysis of SB-RA-2001 in GH161 cells under ATc-induced *ftsZ* KD. (**f**) MIC50-shift analysis of SRI-3072 in a similar experiment. (**g**) Images of *M. bovis* BCG treated with SRI-3072 or SB-RA-2001 at 1x MIC and the vehicle control DMSO, and the cell length differences (n ~100). (**h**) Inhibition of MtbFtsZ GTP hydrolysis by SRI-3072. SBZ-P3G2 was a negative control, as previously reported (Ref. 34). (**i**) First derivative of the thermal-denaturation curve for SRI-3072. MtbFtsZ melting temperature (T_m) was defined at the curve inflection point. The negative ΔT_m of SRI-3072 indicates thermal destabilization of MtbFtsZ. Experimental details of this assay are provided in the Fig. S4 legend.

Figure 1

See image above for figure legend.

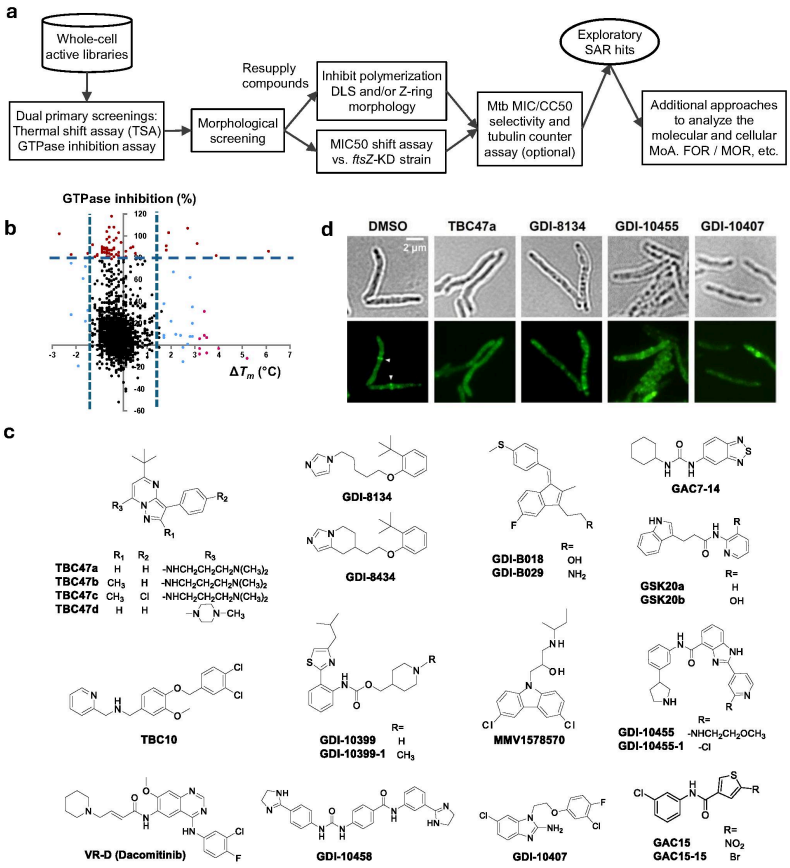


Figure 2. Discovery of *M. tuberculosis* whole-cell active FtsZ compounds from HTS libraries. (**a**) The workflow. (**b**) Primary hits screened by TSA and GTPase inhibition dual assays. (**c**) Structures of the confirmed MtbFtsZ hits. (**d**) Effects of the validated top hits at 1x MIC concentration on Z-ring morphology in *Mycobacterium*. DMSO is the solvent control.

Figure 2

See image above for figure legend.

Figure 3.

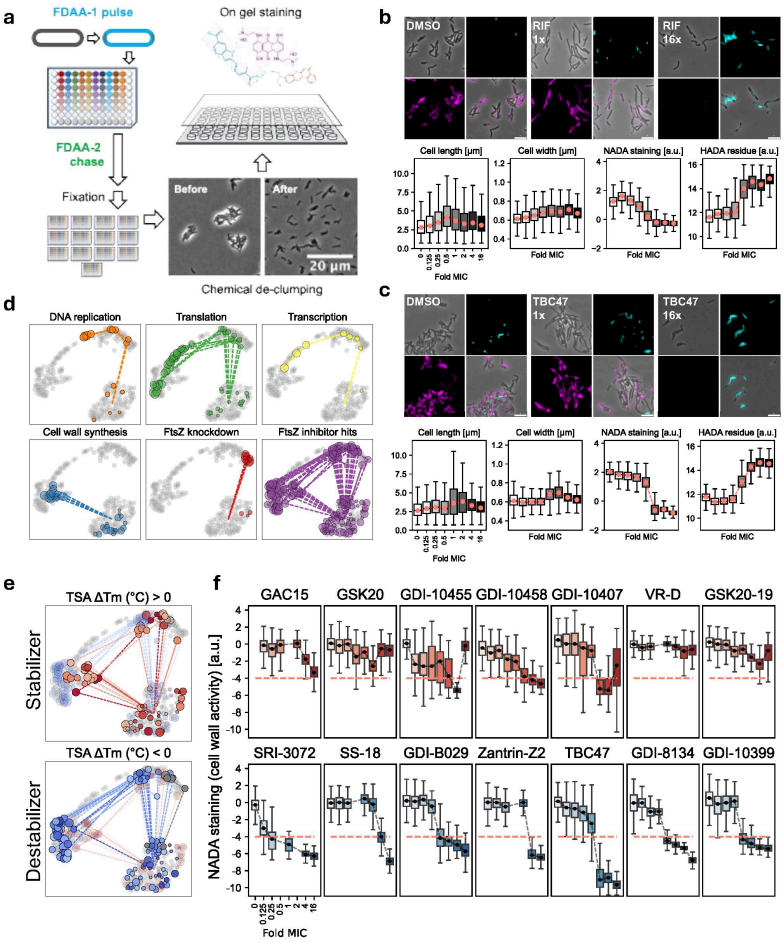


Figure 3. A dual-FDAA pulse–chase-based cytological profiling platform reports drug-induced arrest of cell-wall synthesis and stratifies FtsZ-targeting compounds in BCG. (**a**) Schematic of the high-content imaging workflow. BCG cultures were pulsed with the first fluorescent D-amino acid (HADA; FDAA-1), arrayed into 96-well plates and treated with compounds, chased with the second FDAA (NADA; FDAA-2), fixed, and counterstained (on-gel staining). Bacillary aggregates were chemically de-clumped prior to imaging (representative micrographs before and after de-clumping; scale bar, 20 µm). (**b**, **c**) Representative micrographs and single-cell quantification of BCG treated with DMSO, rifampicin (RIF; B) or TBC47 (C) at 1× and 16× MIC. Phase-contrast, NADA (cyan; de novo peptidoglycan insertion during the chase), HADA (magenta; pre-existing cell-wall label), and merged channels are shown. Box plots depict cell length, cell width, NADA staining intensity, and HADA residue intensity as a function of fold MIC (n ≥ 200 cells per condition; scale bars, 5 µm). (**d**) UMAP embedding of population-level cytological profiles. Dashed trajectories connect increasing compound doses for reference agents grouped by mechanism of action: DNA replication (moxifloxacin, ciprofloxacin; orange), translation inhibitors (amikacin, linezolid, etc.; green), transcription (rifampicin; yellow), cell-wall synthesis (isoniazid, SQ109, SBZ-6B, BTZ-043; blue), genetic FtsZ knockdown (red), and FtsZ inhibitor hits (purple). Grey points denote all other samples. (**e**) Dose-dependent trajectories of FtsZ inhibitor hits on the UMAP, colored by thermal shift assay (TSA) ΔT_m: FtsZ stabilizers ($\Delta T_m > 0$; warm colors) and destabilizers ($\Delta T_m < 0$; cool colors). (**f**) Dose–response of NADA staining (cell-wall synthesis activity) for 14 FtsZ-targeting compounds, stratified as FtsZ stabilizers (top, warm) and destabilizers (bottom, cool). Red dashed line indicates the −4 a.u. threshold for strong inhibition. Box plots show median and interquartile range; red dots mark condition means.

Figure 3

See image above for figure legend.

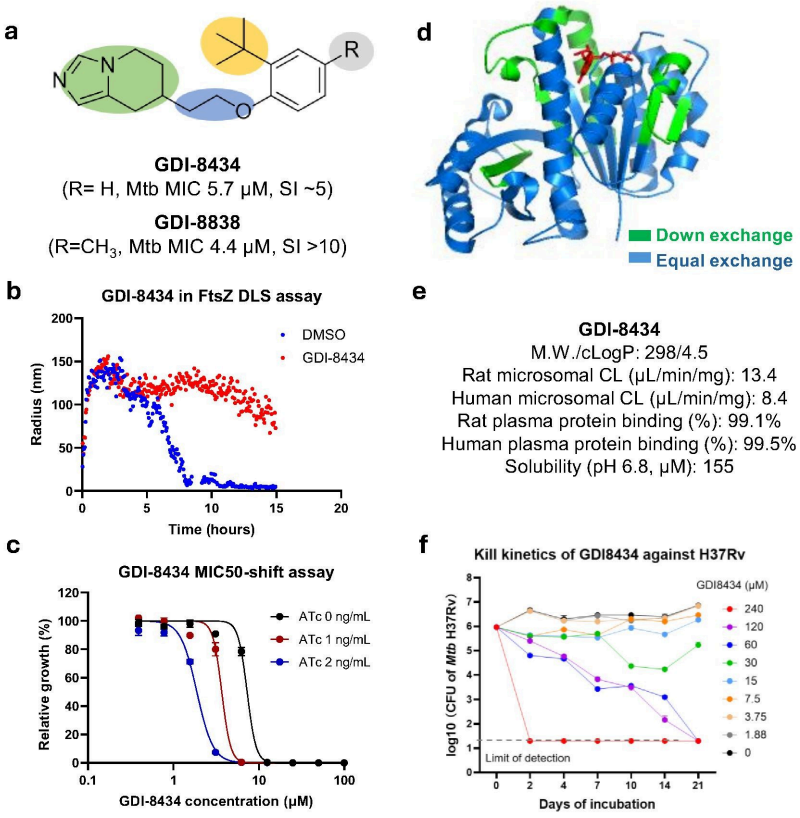


Figure 4. Optimization and evaluation of the MtbFtsZ-destabilizing compound GDI-8434. (**a**) Two representative compounds that were improved from the initial screening hit GDI-8134. The colorings indicate the groups explored by synthesis. (**b**) Dynamic light scattering (DLS) assay of GDI-8434, performed with DynaPro Plate Reader III. (**c**) MIC50-shift assay shows GDI-8434 inhibits MtbFtsZ in cells. (**d**) HDX-MS analysis suggests the peptides (green) in MtbFtsZ exhibit differential deuterium uptake after the protein was incubated with GDI-8434. (**e**) Pharmacological profile of GDI-8434. (**f**) Kill kinetics of GDI-8434 against Mtb H37Rv.

Figure 4

See image above for figure legend.

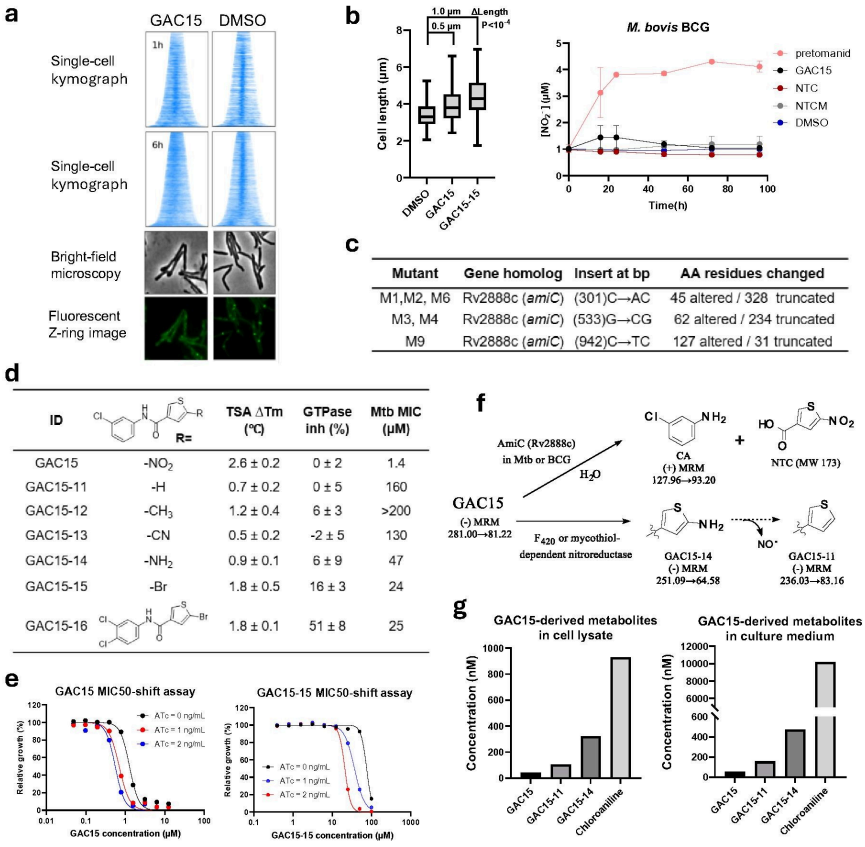


Figure 5. Effects and intracellular metabolism of the FtsZ-stabilizing compound GAC15. (**a**) Fluorescent microscopy images of GAC15 (at 1xMIC) or DMSO-treated mycobacterial cells containing GFP-tagged FtsZ, and the single-cell kymographs, demonstrate the Z-ring morphology.(**b**) Cell length of BCG cells (n ~100) treated with GAC15 at 1xMIC for two days, and nitrite formation of GAC15- and derivative-treated cultures over time. The experiments were repeated twice. Error bars represent the standard error of the mean of triplicate in the Griess assay. (**c**) Isolation of GAC15 resistance mutants and identification of mutations by whole-genome sequencing. The mutants, such as M1, harbor only a single-base insertion mutation that causes a large frameshift identical to ORF Rv2888c (*amiC*) in slowly growing mycobacteria. (**d**) Synthesized GAC15 analogs and their biochemical and biological activities. Data were obtained under the same assay conditions as in Table 1. (**e**) Results of the MIC50-shift assay with GAC15 and GAC15-15. (**f**) Proposed fate of GAC15 and the intramycobacterial metabolites detected. (**g**) Concentrations of GAC-derived metabolites, determined by LC-MS/MS multiple-reaction monitoring (MRM). CA, Chloroaniline; NTC, 5-Nitrothiophene-2-carboxylic acid; NTCM, NTC methyl ester.

Figure 5

See image above for figure legend.

Supplementary Files

This is a list of supplementary files associated with this preprint. Click to download.

- FtsZSI11042026.pdf
- FullgelWBimagesforsupplementaryFigures2and4.pptx
- Table1.jpg